Eur. Phys. J. C (2026) 86:890
https://doi.org/10.1140/epjc/s10052-026-16147-4

THE EUROPEAN PHYSICAL JOURNAL C

Regular Article - Experimental Physics

Design optimization of MAPS-based detectors using a data-driven fast simulation approach

Dumitru Vlad Berlea[1,a], **Lucian Fasselt**[1,2,b], **Prafulla Behera**[3], **Daniela Bortoletto**[4], **Craig Buttar**[5], **Theertha Chembakan**[3], **Valerio Dao**[6], **Ganapati Dash**[3], **Sebastian Haberl**[7], **Tomohiro Inada**[7], **Fuat Kerem Isik**[8], **Cigdem Issever**[1,2], **Xuan Li**[9], **Long Li**[10], **Heinz Pernegger**[7], **Petra Riedler**[7], **Walter Snoeys**[7], **Carlos Solans Sánchez**[7], **Anna Swoboda**[7], **Ilkay Turk Cakir**[8], **Milou van Rijnbach**[7], **Anusree Vijay**[3], **Julian Weick**[7], **Steven Worm**[1,2]

[1] Deutsches Elektronen-Synchrotron DESY, Zeuthen, Germany
[2] Humboldt University of Berlin, Berlin, Germany
[3] Indian Institute of Technology Madras, Chennai, India
[4] University of Oxford, Oxford, UK
[5] University of Glasgow, Glasgow, UK
[6] Stony Brook University, New York, USA
[7] CERN, Geneva, Switzerland
[8] University of Ankara, Ankara, Turkey
[9] Los Alamos National Laboratory, Los Alamos, USA
[10] University of Birmingham, Birmingham, UK

Received: 8 April 2026 / Accepted: 15 July 2026

Abstract A parametric simulation tool for pixel sensors is presented. A realistic pixel response is simulated purely based on measurement input, without requiring detailed knowledge of the underlying manufacturing process. As such, it provides an efficient alternative to the use of Technology Computer-Aided Design simulations, which typically depend on proprietary process information. Due to its parametric approach, the package is fast and thus particularly useful for larger detector systems and high hit rate environments. This work presents measurements, simulation and its validation for the MALTA2 sensor. It is a small collection electrode monolithic active pixel sensor produced in the Tower 180 nm complementary metal-oxide-semiconductor imaging process. Modifications to the sensor's periphery, mainly in the hit merger, are studied in order to optimize the performance for tracking and calorimetry. This optimization is of special interest as part of the MALTA3 sensor redesign in the 65 nm Tower Partners Semiconductor Co. process.

Dumitru Vlad Berlea and Lucian Fasselt have contributed equally to this work.

[a] e-mail: vlad.berlea@desy.de (corresponding author)
[b] e-mail: lucian.fasselt@desy.de (corresponding author)

1 Introduction

The accurate simulation of silicon sensors is essential for the design of next-generation particle physics detectors. This is particularly important for detector components close to the beam pipe of accelerator experiments, such as tracking or vertexing detectors, due to their strict detection requirements. Currently, the most powerful and accurate simulation tools used for optimizing semiconductor detector design are based on Technology Computer-Aided Design (TCAD). Such simulations are the cornerstone for optimizing analog chip design for charge imaging applications. Despite their predictive power, TCAD approaches rely heavily on detailed knowledge of silicon processing parameters, which are often proprietary to the manufacturer or require parameter tuning to data [1,2].

In this paper, we present a design optimization technique for MAPS-based detectors using a parametric simulation. This approach is of special interest for the optimization of the digital read-out of future sensor designs. Different read-out parameters are simulated to improve the tracking performance and digital calorimetry linearity. The simulation does not rely on chip design information, but rather on a parametrization of charge sharing and timing information using test beam and laboratory measurements. Such an approach is well suited for simulations of monolithic active pixel sensors (MAPS), where pixel level digitization is often implemented. The simulation is structured as a GEANT4 suite and C++ analysis package which can be imported and reused for various applications. Currently, the package is considered for several particle physics experiments such as the replacement of the inner layers of the ATLAS inner tracker during the long shutdown 4 period at the high-luminosity LHC [3]. Additionally it is used for the Fast MAPS timing detector for the ePIC experiment at the EIC [4] and position sensitive layers in digital calorimeters.

The fast data driven simulation technique is considered for two applications. First, it enables the optimization of large-scale detector geometries for both tracking and calorimetry applications. Second, the digital read-out can be optimized for future redesigns of MAPS. The latter is investigated in this work, with preliminary suggestions for optimal sensor design being made for the upcoming redesign of the MALTA3 sensor in the 65 nm TPSCo technology node. The sensor will aim to satisfy both tracking and digital calorimetry applications.

Such a simulation could additionally be generalized for other sensors as long as data sets equivalent to what is presented in the following section are acquired.

2 Charge collection measurement

2.1 The MALTA2 sensor

The MALTA2 sensor is the second full-scale prototype of the MALTA sensor family. It is a fully depleted monolithic active pixel sensor (DMAPS) produced in the Tower 180 nm CMOS Imaging Process. It features a 224×512 pixel array with a total active area of 9×18 mm^2. Each pixel has a symmetric 36.4×36.4 µm^2 pitch, with a small octagonal collection electrode (2 µm diameter). MALTA features a fully asynchronous read-out which does not require a clock propagation across the pixel array, leading to optimized power dissipation [5] and timing performance [6].

The sensor read-out architecture consists of 2×8 pixel groups that distribute data packets (40 bit words) across double columns. The digital data comprises binary hit information without time-over-threshold information. The time-of-arrival is added to the hit information off-chip in the read-out through a field programmable gate array (FPGA) with a sampling frequency of 500 MHz. There are 4 additional analog monitoring pixels on both sides of the digital pixel array. They give direct access to the analog waveforms, that is the analog output voltage of the front end amplifier before entering a discriminator.

Several analog process modifications have been investigated over the years in order to primarily optimize the sensor's radiation hardness [7,8]. In this paper, the MALTA2 sample has an epitaxial active volume grown on top of low resistivity silicon, which ensures the mechanical stability of the sensor. The process implements a low dose implant underneath the small collection electrode, which laterally expands the depletion volume across the pixel. An additional process modification adds a gap in the low dose implant, in order to optimize the pixel corner charge collection. Figure 1 shows a schematic of the pixel cross-section.

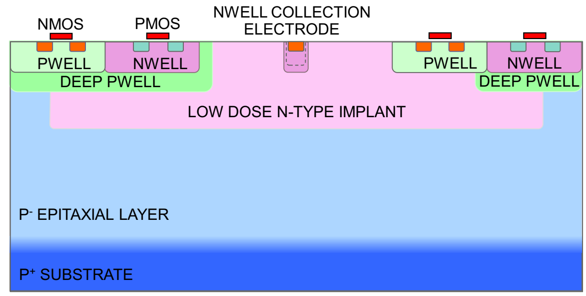

Fig. 1 MALTA2 pixel cross-section on 30 µm thick epitaxial silicon with a gap in the low dose n-type implant. The features of this illustration are not to scale

2.2 Charge sharing model

The parametric simulation presented in this paper is based on a charge sharing model derived from data, obtained via the edge transient-current technique (E-TCT) and test beam at the CERN SPS. Figure 2a shows E-TCT data acquired with a 1064 nm laser by scanning the polished edge of a MALTA2 pixel. The charge amplitude is reconstructed from digital data by measuring the hit occupancy as a function of the detection threshold and interpolating to the threshold at which the occupancy drops to 50% [9,10]. The charge collection model (gray dashed line) is defined as a function of the position x relative to the pixel by:

$$\mathrm{CC}(x; C, \sigma_{\mathrm{erf}}) = \frac{C}{2}\left[\mathrm{erf}\left(\frac{x}{\sigma_{\mathrm{erf}}}\right) - \mathrm{erf}\left(\frac{x-\mathrm{pitch}}{\sigma_{\mathrm{erf}}}\right)\right] \quad (1)$$

C is the normalization constant and σ_{erf} is the width of the error-function that describes the charge collection at the pixel edges. The model is convolved with a Gaussian distribution, which accounts for the smearing due to the width of the laser beam $\sigma_{\mathrm{gauss}} = 4.1$ µm [11]. The convolution (blue line) is fitted to the data. A value of $\sigma_{\mathrm{erf}} = 4.2 \pm 0.6$ µm is obtained for the width parameter of the charge collection model. The measurement on the sensor edge gives access to only one lateral axis (pitch), while the other lateral axis is parallel to the incident laser beam. To test the symmetry of the charge collection, a MALTA2 sensor was also characterized at the CERN SPS with a 120 GeV/c charged hadron beam. In this setup, the beam was incident on the top of the sensor. The charge deposition follows a Landau-distribution. Its most probable value is reconstructed and serves as input for a two-dimensional charge collection model [12]. This is obtained by multiplying two one-dimensional functions:

$$\mathrm{CC}_{2\mathrm{D}}(x, y; C, \sigma_{\mathrm{erf}}) = \mathrm{CC}(x; C, \sigma_{\mathrm{erf}}) \times \mathrm{CC}(y; 1, \sigma_{\mathrm{erf}}). \quad (2)$$

Figure 2b illustrates the two-dimensional model that was reconstructed from test beam data. It is symmetric in x and y and described by:

$$\sigma_{\mathrm{erf}} = 4.3 \pm 0.3\ \mu\mathrm{m} \quad (3)$$

This parameter is compatible with the complementary E-TCT result and serves as the main input for the charge sharing model.

A deposited charge is distributed among the pixel closest to the interaction (the seed pixel) and the three pixels adjacent to the nearest pixel corner. For a charge deposited at local coordinates (x, y) within the seed pixel, the fraction assigned to it is given by $\mathrm{CC}_{2\mathrm{D}}(x, y; C = 1, \sigma_{\mathrm{erf}} = 4.3\ \mu\mathrm{m})$. For the seed pixel, x and y are both inside the base interval [0, pitch]. The charge fractions for the neighboring pixels are obtained by evaluating $\mathrm{CC}_{2\mathrm{D}}$ at coordinates where x and/or y are shifted by one pixel pitch. Consequently, the shifted evaluations are performed outside of the base interval and thus lie in the tails of the charge collection model. Evaluations that are far away from the base interval lead to low charge fractions that will typically fall below the detection threshold. For example, a charge deposition close to the lower left corner of a pixel ($x = 4.0\ \mu\mathrm{m}$ and $y = 1.0\ \mu\mathrm{m}$) leads to the four charge fractions:

$$\begin{aligned} \mathrm{CC}_{2\mathrm{D}}(x, y) &= 0.570 \\ \mathrm{CC}_{2\mathrm{D}}(x, y + \mathrm{pitch}) &= 0.336 \\ \mathrm{CC}_{2\mathrm{D}}(x + \mathrm{pitch}, y) &= 0.059 \\ \mathrm{CC}_{2\mathrm{D}}(x + \mathrm{pitch}, y + \mathrm{pitch}) &= 0.035 \end{aligned} \quad (4)$$

The fractions sum to 1.0. When multiplied with a total charge deposit of $2000\,\mathrm{e}^-$, the pixel charges are $1140\,\mathrm{e}^-$, $672\,\mathrm{e}^-$, $118\,\mathrm{e}^-$ and $70\,\mathrm{e}^-$, respectively. For a detection threshold of $200\,\mathrm{e}^-$ only the first two charges result in a hit above threshold.

By construction, the four resulting fractions sum to unity, neglecting any charge loss effects because the sensitive region is expected to be fully depleted. This approach restricts charge sharing from a single energy deposition to pixel clusters of at most four pixels. Larger clusters may nevertheless arise from multiple ionization processes across different pixels, for example those induced by delta rays. Overall, the model is computationally lightweight, as signal formation only requires the evaluation of a parametric expression. The description of charge collection can be further generalized by including: sharing over more than four pixels; asymmetric behavior by introducing different values for $\sigma_{\mathrm{erf,x}}$ and $\sigma_{\mathrm{erf,y}}$; or implementing an explicit dependence on the z coordinate. For MALTA2 the accurate description of the cluster size is validated in Sect. 4.2.

2.3 Time walk

Pixel sensors for tracking that apply a fixed detection threshold are subject to the time walk effect, thereby introducing a charge-dependent timing shift. In order to obtain a parametric description as simulation input, the voltage amplitude of an analog MALTA2 monitoring pixel is measured with an oscilloscope for different intensities of an infrared laser. Two characteristic waveforms are shown in Fig. 3a for signal charges of 170 and $240\,\mathrm{e}^-$. The oscilloscope is triggered on the rising edge of the laser trigger at a voltage of 1.4 V, which serves as a time reference. The calibration of the waveform is performed by using a charge injection circuit that is inside each pixel. A calibration curve is determined by injecting known amounts of charges and computing the average integral from 5000 waveforms. As a result, a calibrated charge value is obtained for each measured waveform based on its integral. The time of arrival of the device under test ($\mathrm{t}_{\mathrm{DUT}}$) is defined as the time when the waveform crosses a fixed threshold. This detection threshold is set to 140 mV which corresponds to the average amplitude of waveforms calibrated to $150\,\mathrm{e}^-$. For the time walk measurement this corresponding charge threshold of $150\,\mathrm{e}^-$ is chosen because it is typically the lowest operational threshold of a MALTA2 sensor during digital data taking. The time walk curve shown in Fig. 3b is obtained by focusing the laser on the pixel center, varying its intensity and measuring $\mathrm{t}_{\mathrm{DUT}}$ relative to the laser trigger for each injected charge. The fit function diverges when the pixel charge approaches the threshold. For large signals, the time walk curve asymptotically approaches a constant value of 29 ns. The typical charge generated by a minimum-ionizing particle in 30 μm of silicon is $\sim 1800\,\mathrm{e}^-$ [13]. This shows that charge depositions close to a pixel center that are not shared among other pixels are less affected by the time walk. The time walk mainly shifts in time small charge depositions that arise due to charge sharing. As a consequence, pixel clusters show a leading timing from the seed pixel followed by hits from neighboring pixels at later times.

For each threshold value, a different time walk curve is obtained. The measured curve at a threshold of $150\,\mathrm{e}^-$ of Fig. 3b serves as the basis for extrapolation to other thresholds. The time walk curve $\Delta t(x)$ for a collected pixel charge x can be estimated by inserting the threshold value thr into

$$\Delta t(x;\ \mathrm{thr}) = \frac{390\,\mathrm{ns}}{(x\,\frac{150\,\mathrm{e}^-}{\mathrm{thr}} - 149.8)^{0.65}} + 28.6\ \mathrm{ns}. \quad (5)$$

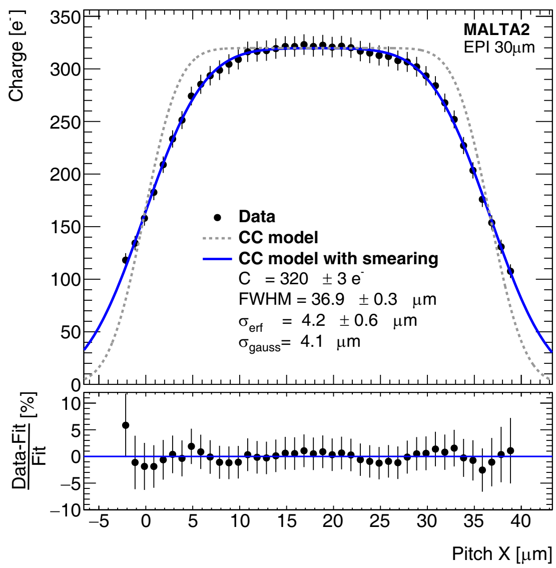

(a) One-dimensional pixel scan via E-TCT.

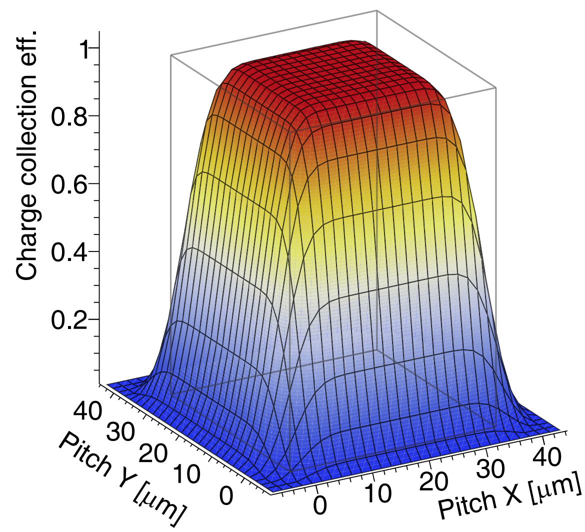

(b) Two-dimensional charge collection model reconstructed from test beam data.

Fig. 2 Charge collection model derived from E-TCT and test beam data. In (**a**) the charge is measured across the pixel pitch by scanning with an infrared laser. The charge collection model (dashed line) describes the data when convolved with the beam width σ_{gauss} (blue line). The error-bars are dominated by the charge calibration of 3%. A two-dimensional charge collection model as illustrated in (**b**) is obtained by charge reconstruction from test beam and is compatible with the E-TCT results. Only the model is plotted. One-dimensional projections of the data can be found in [12]. The gray box illustrates the nominal size of the $36.4 \times 36.4\,\mu\text{m}^2$ pixel

The functional form and parameter values are taken from the fit to the measurement shown in Fig. 3b. The scaling is justified due to the MALTA2 front end design, in which a large threshold range can only be covered by changing the gain of the front end. In this way, the amplification decreases with threshold.

This time walk measurement is based on fixing the position of the laser injection to the pixel center. Consequently, it quantifies the time walk of the front end but neglects contributions to delays in the signal formation such as the drift time from the pixel edges to the center. The pixel is assumed to be fully depleted and the drift time is small compared to the time walk of the front end [14].

2.4 Digital hit merging

In the MALTA2 read-out hits are merged in the digital circuit if they arrive within the same time window of 1.6 ns. While merging leads to data reduction, it also introduces a source of in-efficiency. In the following, the implementation of the digital read-out is presented. A quantitative study of the inefficiencies follows in Sect. 4.1 and a proposed design optimization in Sect. 5.1.

The implementation of the MALTA2 asynchronous read-out requires a sub-division of the pixel matrix into double columns, which are further divided in 2×8 pixel groups. A hit above threshold triggers a 40 bit MALTA word. Its composition of the 30 relevant bits for this work is listed in Table 1. Hits within the same group can be read out in one MALTA word. The corresponding pixel position is encoded by a 1 in the pixel address. The group and double column positions are encoded using 14 additional bits.

Each double column features two independent column drain buses that connect the pixel groups to the sensor periphery, dependent on their parity. In total, the sensor contains 256 double columns and 512 column busses. Each bus operates independently, however it drains into a common 40-bit wide parallel bus. All words arriving within the same 1.6 ns time window on this common bus are merged by a bit-wise OR gate and are read out in parallel off-chip.

Figure 4 illustrates three cases of hit merging: no-loss merging, displaced merging and hit loss merging. Each hit is associated with a MALTA word that encodes its position in the in-pixel circuitry. The 16 most significant bits one-hot encode the pixel address. The next 5 bits encode the group address and the next 1 bit the group parity. The 8 least significant bits encode the double column address. In the first case (left) the two hits are detected in the same 2×8 pixel group and are merged correctly because their encoding only differs in the pixel address. A cluster of two hits that spreads over different pixel groups (middle) is merged to

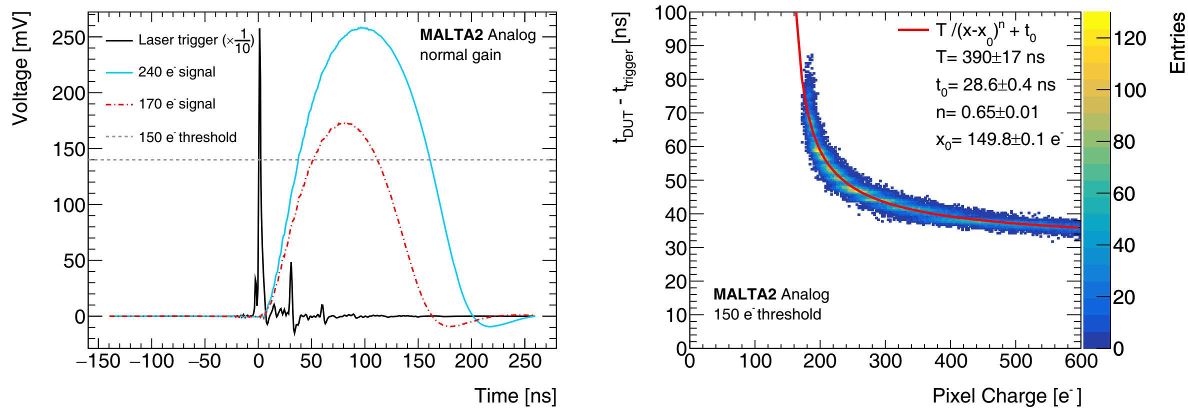

(a) Analog waveforms. (b) Time walk curve at a threshold of $150\,e^-$.

Fig. 3 Analog waveforms (**a**) are acquired with dedicated analog monitoring pixels of MALTA2 for different laser intensities with an E-TCT setup. The time walk relative to the laser trigger is shown in (**b**)

two displaced hits. Any two hits with the same pixel address (right) are merged to form a single hit which can be displaced.

Experimentally, the merging can be studied through E-TCT by inducing a signal at the boundary of two pixel groups. A one dimensional scan across the pitch axis is shown in Fig. 5a covering pixels from column 0 to 16. Due to a slight inter-pixel gain variation in the analog front end, the maximum charge varies by an order of 10% between pixels. Figure 5a also shows that a similar charge distribution is retrieved for each pixel with values of the FWHM compatible with the pixel pitch (36.4 µm). Dashed lines mark the boundaries between pixel groups that are defined by the double-column arrangement. Figure 5b shows the same dataset and highlights the data points that fall at least one pixel pitch away from the expected pixel center. All of these points are associated to displaced merging occurring at the boundary between pixel groups. In this case, the dominant merging effect is in the 8 bit long double column ID. Table 2 provides a visual aid to the displaced merging observed in the E-TCT data. It summarizes the column coordinate of two neighboring pixels and their double column ID in binary representation. The same double column ID is shared by two neighboring columns in the same pixel group defined by the integer division

$$\text{dcol} = \text{column}/2. \tag{6}$$

The merging between neighboring groups has a systematic pattern. All the displaced hits marked with bold in Table 2 are observed in the highlighted data of Fig. 5b. Every second group boundary leads to a single displaced hit (e.g. columns 1,2 → 2,3) where one hit remains unchanged. Consequently, this surviving hit is still efficiently detected. Every other boundary leads to two displaced hits (e.g. columns 3,4 → 6,7). Such merging introduces detection inefficiencies if the displacement of both hits is larger than a specified tracking cut.

Table 1 The MALTA word composition of the 30 bits encoding a hit. From the full 40 bit MALTA word only the 30 relevant bits for the hit merging discussed in this work are listed. For simplicity, the bits representing a reference, delay count, bunch crossing ID and chip ID are omitted here

Bits	Size	Description
0-15	16	Pixel address in 2 × 8 pixel group
16-20	5	Group address
21	1	Parity (0 or 1)
22-29	8	Double column ID (up to 256)

The merging has been tested for the specific case of scanning across the column axis of a MALTA2 sensor. The appearance of displaced hits is explained by the digital hit merging which can introduce detection inefficiencies. The effect of the merger onto the sensor efficiency will be discussed in Sect. 4.1 and on the cluster size in Sect. 4.2.

3 The simulation approach

The simulation package is structured in two distinct parts: the GEANT4 simulation and the C++ analysis. The GEANT4 simulation design principles revolve around a scalable and time efficient simulation (10 kEvents/s), while most computationally intensive tasks are relegated to the analysis. This allows for an optimized work flow for investigating different sensor parameters and allows for efficient device scaling for large detector simulations.

3.1 GEANT4 simulation

The GEANT4 simulation implements a MAPS sensor as a monolithic silicon block with the dimension of the sensor's sensitive volume. The silicon pixelation is applied for

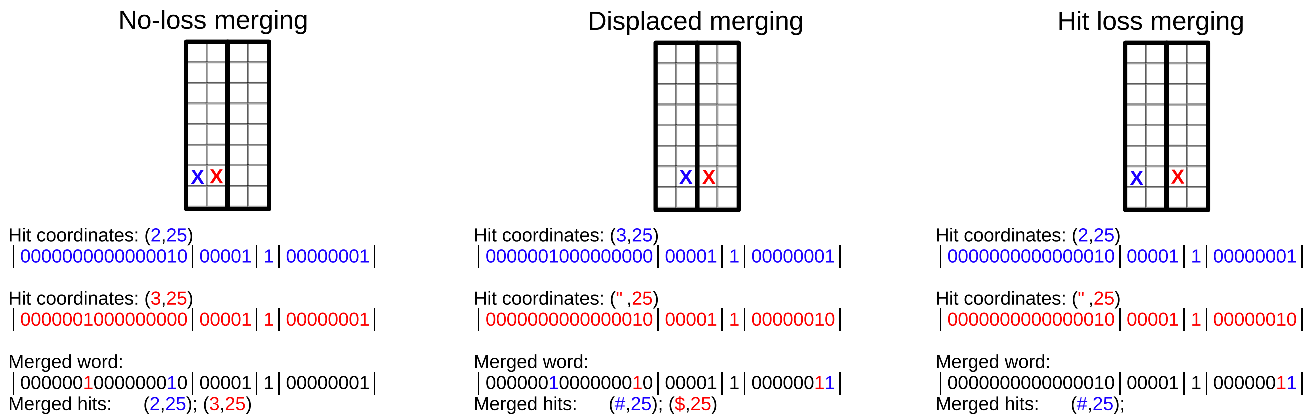

Fig. 4 Examples of merging of hits arriving within 1.6 ns: No-loss merging (left), Displaced merging (middle) and Hit-loss merging (right). Each hit is associated with a 40 bit word that encodes its position in the in-pixel circuitry. In the illustration, a reduced 30 bit word is shown, associated to the minimum amount of bits needed to encode a pixel position in the MALTA2 matrix. For clarity, each bit group is delimited by vertical bars and follows the composition listed in Table 1

Fig. 5 Reconstructed charge of pixels within one row of a MALTA2 sensor measured with an E-TCT setup while scanning the pitch axis. (**a**) shows all reconstructed pixel charges. (**b**) highlights those data points that arise at least one pixel pitch displaced from the expected pixel center. Dashed lines indicate the boundary of double-columns. It is observed that displaced charge values appear at these boundaries due to hit merging. The appearance of data from columns 30 and 31 is only due to merging. Table 2 summarizes all merged hits

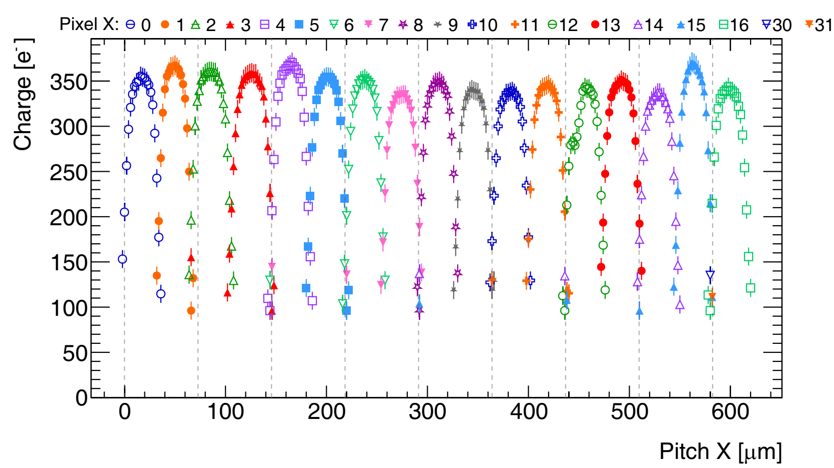

(a) Results of a pitch axis scan across pixels from column 0 to 16

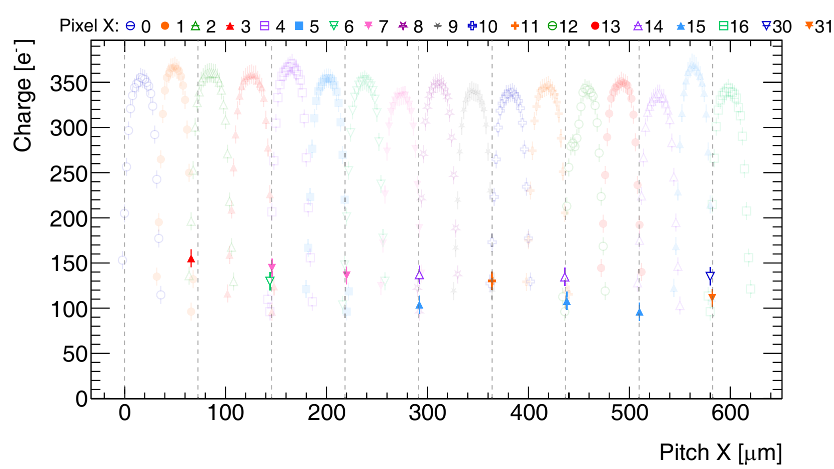

(b) Highlighted results of a pitch axis scan of hits appearing due to merging.

Table 2 Hit merging across different double columns. Two pixel hits from neighboring columns are merged to output hits at different pixel coordinates. The 4 least significant bits of the 8-bit double column IDs of both hits are listed. The upper 4 bits are zero and thus omitted. A bitwise OR operation is performed in the merger. From the resulting double column ID, the corresponding merged column coordinates are obtained. These columns always lie next to each other inside the same double column as they share the same MALTA word. In bold are marked the output columns corresponding to displaced hits that are observed in Fig. 5

Hit column input	Double column ID OR operation	Merged column output
1, 2	0000 | 0001 → 0001	2, **3**
3, 4	0001 | 0010 → 0011	**6**, **7**
5, 6	0010 | 0011 → 0011	6, **7**
7, 8	0011 | 0100 → 0111	**14**, **15**
9, 10	0100 | 0101 → 0101	10, **11**
11, 12	0101 | 0110 → 0111	**14**, **15**
13, 14	0110 | 0111 → 0111	14, **15**
15, 16	0111 | 1000 → 1111	**30**, **31**

each GEANT4 step together with the charge sharing model presented in Sect. 2.2 and the time corrections presented in Sect. 2.3.

The particle gun implementation assumes a monoenergetic beam population. This assumption does not match exactly the experimental conditions of the SPS mixed hadron beam (120–180 GeV mixed hadrons). The impact of the discrepancy on the data-to-simulation comparison is expected to be negligible. This is because a similar, minimum-ionizing energy deposition is expected for hadrons in this energy range in thin silicon substrates ($\sim 30\ \mu$m).

In all simulations, except of Fig. 18 no beam divergence is implemented; as a consequence all primary particles are exactly perpendicular to the sensitive volume. Secondary particles can nonetheless be generated and propagate at large angles (e.g. delta rays). The impact of non-perpendicular primary particles is not found to be large as will be discussed in Sect. 5.1.

The energy deposition of the primary particles is considered only in the defined sensitive volume. The thickness of this was derived from E-TCT [11] and test beam measurements [9]. This is because with an epitaxial layer of $\sim 30\ \mu$m grown on top of a low-resistivity substrate, almost no signal contribution is expected from the substrate. Both electromagnetic (G4EmStandardPhysics Class) and hadronic (G4HadronElasticPhysics Class and G4HadronPhysicsFTFP_BERT Class) interactions are considered, although due to the choice of primary particles (protons and electrons), the dominating effects are due to electromagnetic interactions in silicon. The deposited energy is next converted to electron–hole pairs [15]. The charge sharing between neighboring pixels is done for each GEANT4 step ($1\ \mu$m step) using the parametrization in Sect. 2.2. Lastly, the charge integration for each pixel is performed by summing up all individual GEANT4 steps. A global time stamp is derived from the first GEANT4 step at which the pixel charge exceeds the threshold.

The particle gun implements a configurable particle frequency which allows for simulating the effect of particle pile-up.

In the following study, the simulation of a MAPS for tracking and for digital calorimetry has been performed. Their implementation in GEANT4 is discussed below.

3.1.1 Tracking simulation

The tracking simulation mainly aims to validate the chosen charge sharing model against experimental data. In order to more accurately recreate the test beam conditions, six passive tracking planes have been implemented as bare silicon blocks, three before the device under test and three after. Their positions were implemented based on the real telescope arrangement.

The particle gun aims to resemble the average particle content and energy recorded during the numerous test beam experiments with the MALTA telescope [16] in the SPS beam line. As such 120 GeV/c protons have been chosen as the primary particle. In order to avoid position biases, the beam has a uniform distribution across the sensor.

3.1.2 Digital calorimetry simulation

The simulation of MAPS for digital calorimetry is achieved by implementing a 3.2 cm thick tungsten block in front of

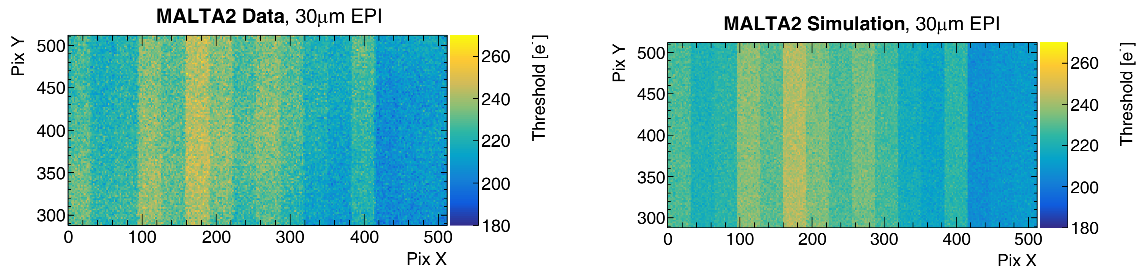

(a) Data. (b) Simulation.

Fig. 6 Two-dimensional threshold distribution across a MALTA2 sensor. The pattern arises due to the on-chip current mirror placement that ensures a uniform propagation of the bias voltage across the sensor

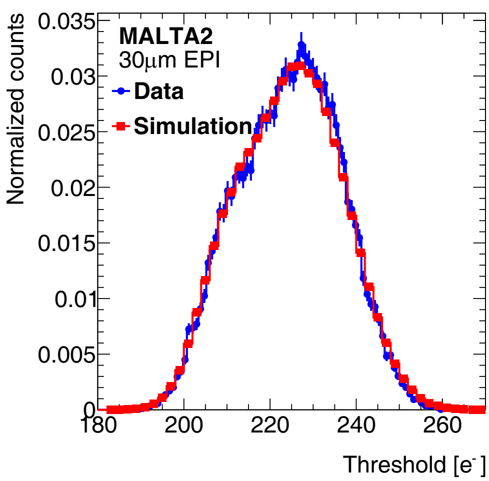

Fig. 7 Distribution of threshold values for data (blue line and points) and simulation (red line and points)

the sensor. The tungsten thickness corresponds to 9 X_0, that is the depth at which an electromagnetic shower induced by an electron of 120 GeV reaches its maximum. This will then provide a worst case analysis of the saturation effect of the energy measurement because at this depth the hit density is at its maximum.

The primary particles are electrons in order to consider only the effects of the electromagnetic showers with varying monoenergetic distributions between 5–100 GeV. In order to limit the effect of the shower leakage, a narrow Gaussian electron beam of 100 μm width centered on the sensor was chosen.

3.2 Analysis

The tracking analysis performed on the simulation output (position, time and energy) is functionally divided into five parts (1–5): digitization, timing, tracking, clustering and analysis. The calorimetry analysis contains only 3 steps: (1, 2 and 5): digitization, timing and calorimetry. All these steps are further detailed below.

1. *Digitization.* Each pixel charge is evaluated against its threshold. A full chip threshold distribution for both data and simulation can be seen in Fig. 6. The visible column pattern is well documented [5] and associated to the current mirrors present every 32 columns in order to propagate the bias voltage across the sensor. The threshold dispersion varies chip-to-chip, but remains constant in time for one sensor. The simulation implements a random threshold distribution, however the mean for each 32 column block was tuned to data and fixed for this particular data-to-simulation comparison. The threshold modeling is important in order to accurately describe the 10 % dispersion in the threshold distribution observed in data [8]. The agreement between data and simulation can also be observed in the threshold distribution of Fig. 7. A generalization of this threshold dispersion is implemented by randomizing based on the dispersion.
   All charge depositions above the pixel threshold are considered as hits and are then encoded in terms of their pixel coordinates and time stamp according to the MALTA2 bit encoding. The merging logic described in Sect. 2.4 is applied, followed by the decoding logic of the new pixel coordinates.
2. *Timing.* The hit timing includes several contributions: time walk, row propagation, front end jitter and the FPGA sampling jitter. The time walk effect is described in Sect. 2.3 and is the main charge-dependent time component. The row propagation is due to the buffering time of hits along the matrix column drain. A maximum of 7 ns accumulates when passing a hit along all 512 rows of a MALTA sensor. This leads to a corresponding delay per row of 0.0137 ns [17]. It has an impact on the merging rate and is subtracted as a constant offset from any timing result. The front end and FPGA sampling jitter are the only irreducible noise components considered for the timing of the sensor [6].

3. *Tracking.* All decoded hits are matched to the primary particle tracked through the telescope set-up. The matching occurs in a fixed time window of 500 ns and spatial window of 100 μm (∼ 3 pixels). These values resemble the test beam analysis conditions.
4. *Clustering.* Hits matched within the same time window undergo a clustering algorithm that checks for the formation of valid clusters, as defined in Reference [18]. Compatible to the test beam analysis, pixel clusters can only be formed from adjacent hits. Additionally, each cluster is endowed with a cluster timing, associated to the earliest hit.
5. *Analysis.* Tracking figures of merit are computed: efficiency, cluster size and timing.
6. *Calorimetry.* The decoded hit coordinates are matched to a primary particle if they fall in a time window defined by the beam frequency. The resulting number of secondary hits is then computed.

3.3 Figures of merit

The main figures of merit for tracking applications are the sensor efficiency, cluster size and timing. The definition of these is compatible with previous definitions used in works describing the performance of the MALTA sensor [17].

The average sensor efficiency is deduced as the ratio between hit-matched tracks and all tracks. The cluster size is defined as the average number of spatial- and time-adjacent hits associated to a single track. It provides a direct validation of the charge sharing model. The cluster timing is defined as the fastest hit within a cluster relative to the creation of the primary particle in simulation and relative to a scintillator trigger in data. The time resolution is computed as the standard deviation of the cluster timing distribution. This figure of merit provides validation for the implemented timing model. The center to corner timing difference provides a complementary quantitative check on the in-pixel distribution.

For the digital calorimetry application, the only figure of merit considered in this work is the number of detected secondaries (hits per event) which is approximately proportional to the energy of the primary scattered particle.

All plots include error bars given by the statistical uncertainty. Due to the large number of statistics in both data and simulation, these are often hidden by the marker size.

4 Simulation validation

The validation of the simulation has been performed with the help of complementary test beam data. The data was acquired with the MALTA telescope [16] in the SPS beam line. A mixed beam of hadrons with energies around 120 GeV was used.

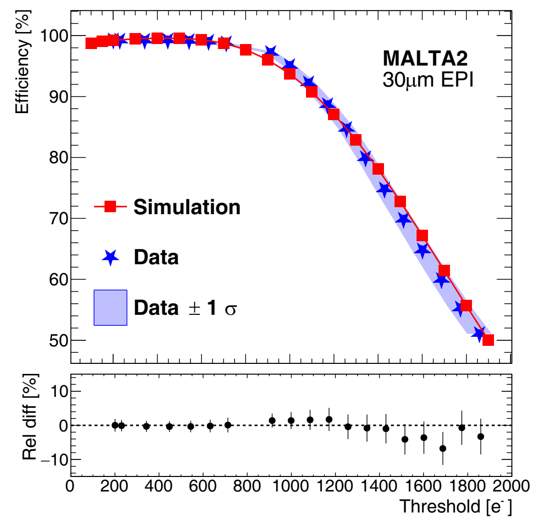

Fig. 8 Detection efficiency for various threshold sensor configurations. With blue, data from the SPS test beam is plotted together with a 1 sigma band dominated by the 3% threshold uncertainty. With red, the simulation output is plotted. The relative data-simulation residual is plotted in the lower panel

The primary tracking figures of merit have been investigated for both data and simulation in order to showcase the realism of the simulation: detection efficiency, cluster size and cluster timing.

4.1 Sensor efficiency validation

Figure 8 shows the efficiency for several threshold settings spanning the entire dynamic range of the sensor (200–2000 e^-). The data points have been obtained for the same sample, however in order to cover the large threshold range, two different front end configurations have been used, corresponding to a high and low gain configuration respectively [9]. A good match between data (blue stars) and simulation (red squares and line interpolation) is obtained within a 1σ band, dominated by the 3 % threshold uncertainty [10]. A relative difference in efficiency within ± 2 % is gained for a sensor threshold below 800 e^-. There is a slight over-estimation of the efficiency in the simulation for sensor thresholds above 1200 e^-.

Of particular interest is the nominal operational threshold of 200 e^- applied to MALTA2 samples. For this particular sensor setting, an average efficiency of 99.24 ± 0.01 % is obtained for data and 99.23 ± 0.01 % for simulation. While the charge collection efficiency is expected to reach a value > 99.8 % at the pixel center, the lower efficiency measured and simulated is associated to the inefficiencies of the merging circuit. This highlights the accurate simulation of the merging circuit effect on the sensor's figures of merit. Figure 9 (a) and (b) shows the efficiency for data and simulation respectively

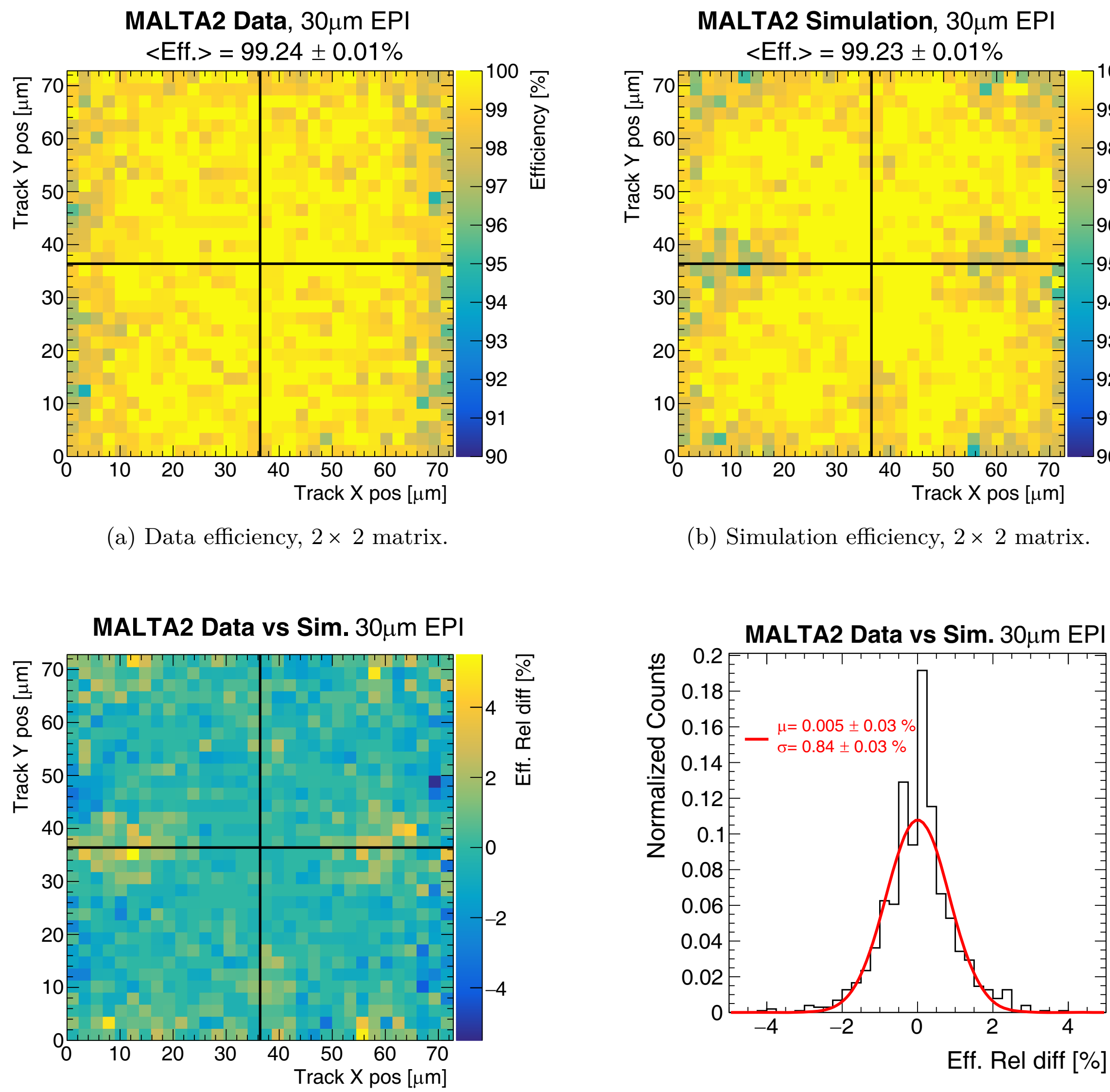

(a) Data efficiency, 2 × 2 matrix.

(b) Simulation efficiency, 2 × 2 matrix.

(c) Relative data-simulation efficiency residual, 2 × 2 matrix.

(d) Relative data-simulation efficiency residual distribution.

Fig. 9 Efficiency projected onto a 2 × 2 pixel matrix for data (**a**) and simulation (**b**). Both plots correspond to a sensor threshold of 200 e^-. An average efficiency of 99.24 ± 0.01% was measured for data and 99.23 ± 0.01% for the simulation. The relative efficiency residual between data and simulation projected onto a 2 × 2 pixel matrix is shown in (**c**). The distribution of the relative efficiency residual between data and simulation is shown in (**d**). A gaussian fit is plotted with red yielding a mean of 0.005 % and an error on the mean of 0.03%

projected within a 2 × 2 pixel array. The number of simulated events has been chosen to match those in data. At the center of the pixel group, an efficiency > 99.98% is gained for both simulation and data, matching the expectation of a fully depleted sensitive volume [1]. The inefficient in-pixel regions for both simulation and data are compatible with the displaced merging effect which occurs at the boundary of the 2 × 8 pixel groups but not within. A simulation with an increased number of events is also presented in Fig. 10 which shows a projection onto the full 2 × 8 pixel group. A loss in efficiency is dominant in the corner of the group.

Figure 9 (c) shows the two dimensional bin-to-bin comparison between simulation and data. No significant pattern is observed within an overall variation of ±5 %. Figure 9 (d) showcases the one dimensional distribution of the data and simulation residual. A gaussian fit (red line) to the residual highlights a mean value of 0.005 ± 0.03 %, which verifies the hit merger to equally affect data and simulation.

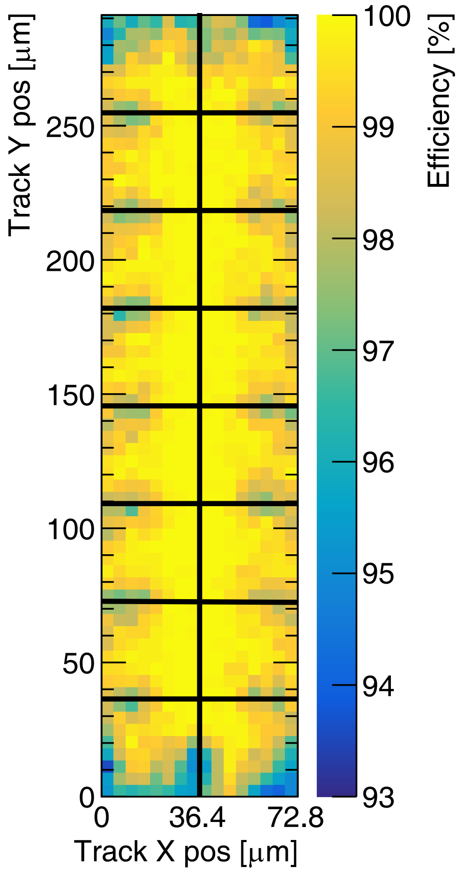

Fig. 10 Simulated efficiency projected onto a 2×8 pixel matrix at a threshold of $200\,e^-$. The matrix matches the size of a single MALTA pixel group

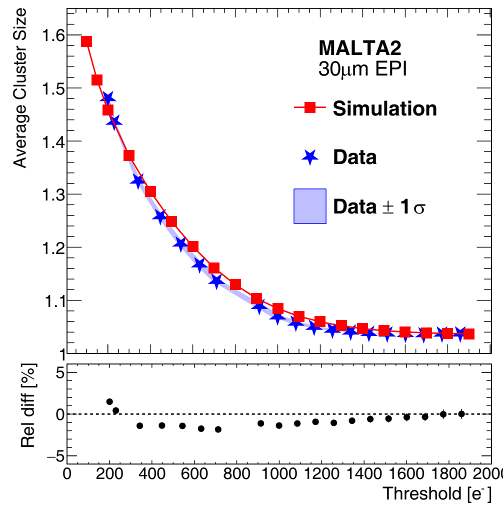

Fig. 11 Average cluster size for various threshold settings. With blue, data from the SPS test beam is plotted together with a 1 sigma band dominated by the 3% threshold uncertainty. With red, the simulation output is plotted. The relative data-sim residual is plotted in the lower panel

4.2 Cluster size validation

A similar study has been performed for the average cluster size. Figure 11 shows the average cluster size for several sensor threshold settings. A good match (within $1\,\sigma$) has been obtained between data (blue stars) and simulation (red squares and interpolated line). The computed residual additionally showcases a data to simulation variation within $\pm 5\%$ across all threshold settings.

Considering the operational threshold of $200\,e^-$, the 2×2 pixel projections for data and simulation are shown in Fig. 12(a) and (b). A quantitative match between the two is obtained: an average cluster size of 1.48 ± 0.01 pixels is obtained for data, while the simulation records a value of 1.45 ± 0.01 pixels. The qualitative match between the two is apparent, however a more descriptive image of the residual distribution is obtained in Fig. 12(c). No significant pattern is observed, however a larger bin-to-bin variation is recorded compared to the efficiency residual in Fig. 9(c). A quantitative analysis of the residual is performed in Fig. 12(d) where an average value of $1.67 \pm 0.12\,\%$ was obtained. This highlights that the simulated cluster size is compatible with data within a deviation of $2\,\%$.

4.3 Timing validation

Figure 13 shows the 2×2 in-pixel cluster timing distributions for data and simulation. The average timing across the whole sensor is subtracted from each bin. The red boxes denote the bins considered in the computation of the average center and corner timing respectively. The shape of the in-pixel cluster timing distribution is well reproduced by the simulation. At the pixel edges, the cluster timing increases due to a smaller collected charge leading to a larger time walk. A center to corner timing difference of 3.12 ± 0.11 ns is obtained for data, while a value of 1.38 ± 0.11 ns is obtained for the simulation. This highlights that the two do not have an exact quantitative match. This can be due to differences between tested sensors and their environments. The time walk curve is measured on an analog test pixel with laser injection. It depends on the gain of the front end which depends on the bias settings and temperature. Figure 5a already shows a $\sim 10\%$ change in gain between different pixels, which can explain the observed discrepancy in the simulation. Additionally, the drift time of charges from the pixel corner to the electrode is not considered in simulation which could lead to an underestimation of the corner timing in simulation.

To understand the impact of the data to simulation timing mismatch, the distribution of cluster timing for both was investigated in Fig. 14. The simulation accurately captures both the gaussian core of the time distribution as well as the

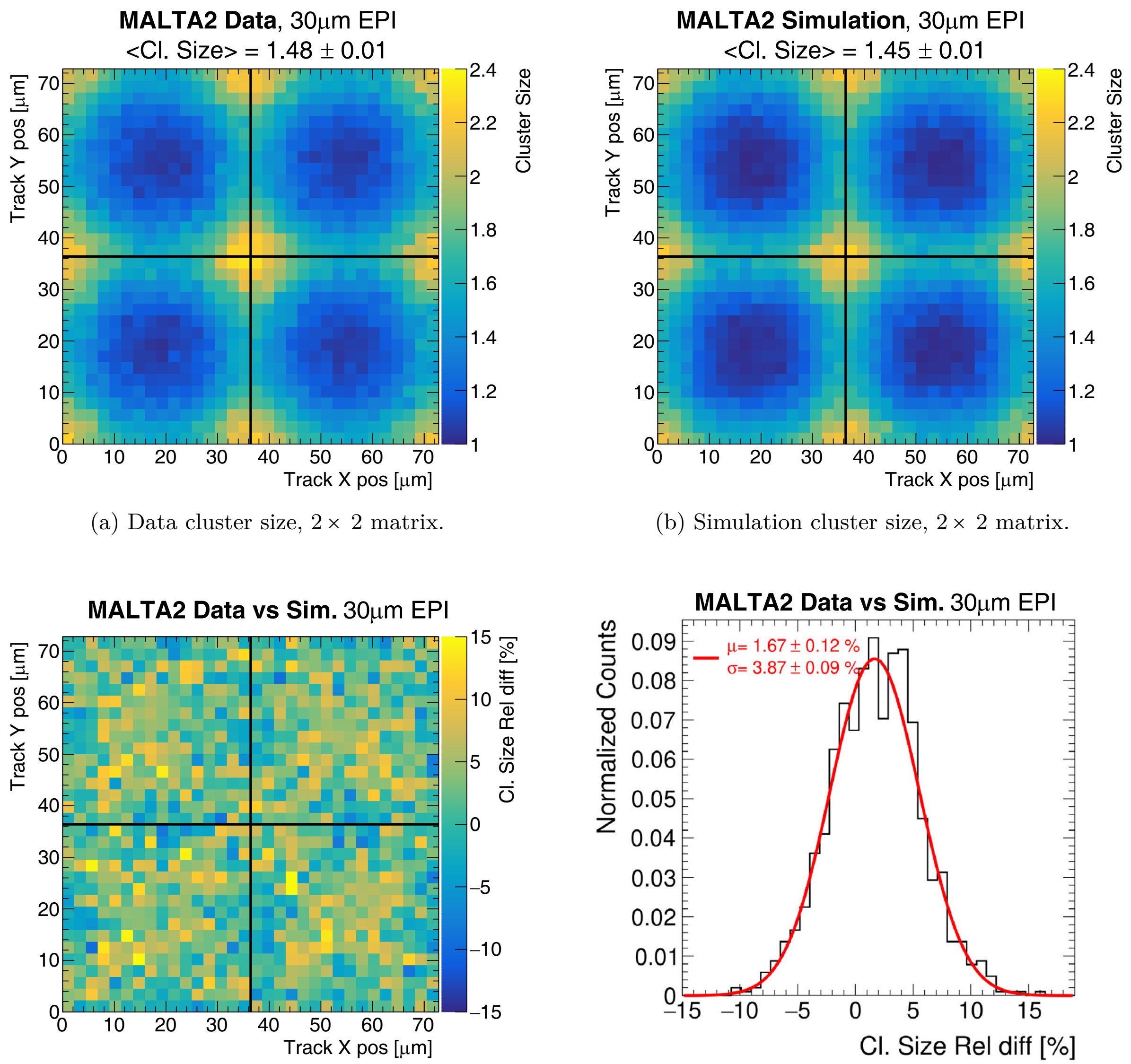

(a) Data cluster size, 2 × 2 matrix.

(b) Simulation cluster size, 2 × 2 matrix.

(c) Relative data-simulation cluster size residual, 2 × 2 matrix.

(d) Relative data-simulation cluster size residual distribution.

Fig. 12 Cluster Size projected onto a 2 × 2 pixel matrix for data (**a**) and simulation (**b**). Both plots correspond to a sensor threshold of 200 e^-. An average cluster size of 1.48 ± 0.01 pixels was measured for the data and 1.45 ± 0.01 pixels for the simulation. The relative cluster size residual between data and simulation projected onto a 2 × 2 pixel matrix is shown in (**c**). The distribution of relative cluster size residual between data and simulation is shown in (**d**). A gaussian fit (red line) yields a mean of 1.67 % and an error on the mean of 0.12 %

tail at larger time values. An offset was introduced in the simulation, such that the mean of the distribution is compatible with data. A time resolution of 2.5 ns was recorded for the data and 2.4 ns for the simulation. This showcases that while variations between data and simulation in terms of the implemented time walk model exist, their contribution to the time resolution is not significant. The time resolution in both data and simulation is dominated by the analog and sampling jitter.

5 Digital front end simulation testbed

The MALTA2 sensor is planned to be redesigned in the 65 nm feature size TPSCo technology [19], in order to benefit from the increased intrinsic radiation hardness and front end active element density. The redesign will significantly alter the analog properties of the sensor and as a consequence the input data used in the parametric simulation [20]. A future validation of this work will need to be performed with test beam and E-TCT measurements on 65 nm demonstrators. The con-

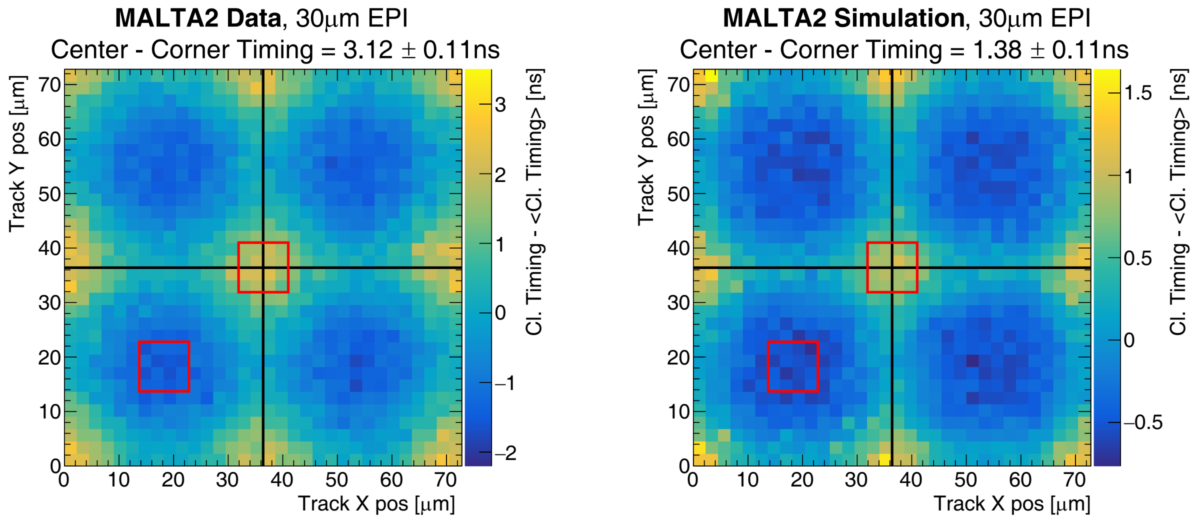

Fig. 13 Average subtracted cluster timing projected onto a 2×2 pixel matrix for data (left) and simulation (right). Both the data and simulation correspond to 200 e^- threshold. The center to corner timing difference was computed using the bins indicated by the 2 red squares. A value of 3.12 ± 0.11 ns was obtained for the data and 1.38 ± 0.11 ns for the simulation

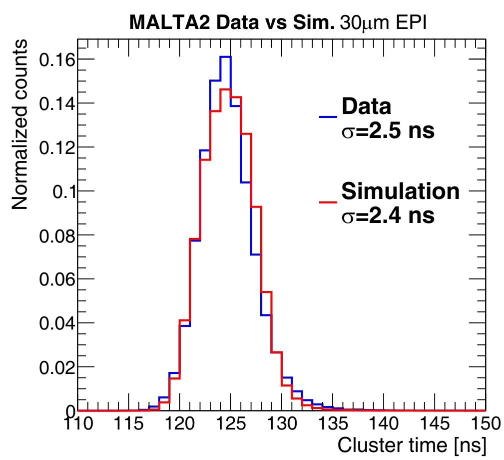

Fig. 14 Distribution of cluster timing for both data (blue line) and simulation (red line). Both the data and simulation correspond to 200 e^- threshold. The timing resolution is derived from the gaussian fit of each distribution. A value of 2.5 ns is obtained for the data and 2.4 ns for the simulation

clusions on the digital circuit however are agnostic to the feature size, as digital blocks functionality is mostly compatible between designs. As a consequence, conclusions on the digital read-out remain of interest for future sensor designs.

A key part of the redesign is addressing the main inefficiencies of the previous sensor iterations and bringing improvements to the design of the digital read-out. In this study we performed an investigation of different digital front end parameters in order to gauge the current design limitations and possible improvements for future MAPS. The range for the sensor digital parameters was chosen in order to maintain a realistic sensor design (pixel grouping size and merging window size).

The MALTA sensor employs an asynchronous read-out in order to optimize the timing performance and power dissipation. An unintended consequence of an asynchronous read-out is the requirement of prioritizing or gracefully merging multiple coincidental hits at the sensor's periphery. As was already shown in the previous sections, the multiple hit handling can introduce inefficiencies with different impacts depending on the sensor settings or beam conditions. With the advent of new and more demanding experimental requirements [21], more MAPS design projects are considering the implementation of an asynchronous read-out. As a consequence, the simulation work provided in this section holds a significant value for the design of future sensors.

Two different physics cases have been considered in the context of proposing new asynchronous read-out sensors: tracking and digital calorimetry. Each case is further discussed individually.

5.1 Tracking application

MAPS for tracking applications require sub pixel position resolution. As a consequence, large pixel coordinate shifts due to the merging circuit can introduce position resolution degradation. The same effect is expected to degrade the detection efficiency when hits are merged away by 3 or more pixels ($> 100\,\mu$m).

One of the most important sensor parameters that is expected to impact the merging inefficiency is the merging window size. This value is inversely proportional to the

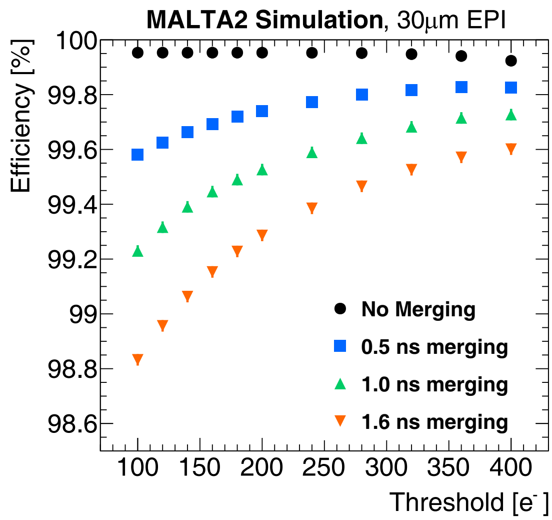

Fig. 15 Simulation of efficiency for various sensor threshold settings. The different curves correspond to various merging time windows. The time window corresponding to the no merging, functionally denotes the idealized case of a 0 ns merging window. All simulation points correspond to a 2×8 pixel grouping

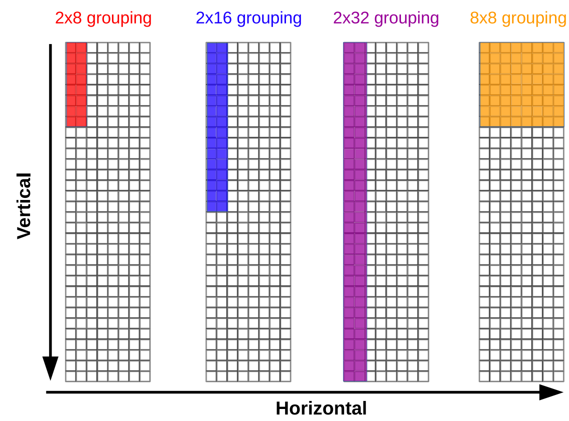

Fig. 16 Pixel grouping illustration. The 2×8 pixel group is the one implemented in the MALTA2 sensor. Other groupings are studied in order to reduce the effect of the merging logic when merging hits from different groups

merging frequency in the periphery. Figure 15 shows the simulated efficiency for several thresholds within the expected operational range of a MALTA2 sensor (below 400 e$^-$) [10]. The several sets of points represent different merging window sizes ranging from the 1.6 ns (orange triangles) which matches the current sensor implementation, to the no merging implementation (black points) representing an ideal case where an infinite merging frequency is used in the read-out. A slight efficiency decrease ($\sim 0.05\%$) at thresholds above 400 e$^-$ is caused by charge depositions at a pixel corner that get equally shared among its neighbors and thus fall below threshold. A systematic decrease in efficiency with an increase in the merging time window is explained by an increased time coincidence between time adjacent hits (shared charge or multiple primary particles). An increase in efficiency is gained with relatively higher thresholds up to a plateau ($\sim$ 400 e$^-$), due to the inefficiencies being dominated by the merging of neighboring hits from charge sharing. Higher thresholds decrease the average cluster size as can be seen in Fig. 11, leading to less frequent merging. Additionally, due to the interplay between timing and threshold, discussed in Sect. 2.3 and highlighted in Eq. 5, larger thresholds on average are associated to a larger time walk for spatially adjacent hits, leading to less frequent merging. A merging time window of 0.5 ns operated at a threshold of $\sim$ 100 e$^-$ leads to a significant efficiency improvement $> 99.6\,\%$.

Another strategy for mitigating the merging effect is by varying the pixel grouping in the read-out. The merging time was kept at the default value of 1.6 ns. Figure 17 investigates the impact on the efficiency of pixel groupings of various sizes from the current design 2×8 pixel groups (red squares), to larger column groups of 2×32 (purple triangles) and also an 8×8 pad pixel group layout (orange crosses). These groupings are illustrated in Fig. 16. A larger pixel grouping is associated with an increase in efficiency. An additional effect can be observed for the 8×8 pixel grouping, where an increase in efficiency is gained over the 2×32 configuration. Both highlighted effects can be understood from geometrical considerations. Hit merging happens only between neighboring pixel groups, scaling with the perimeter of the group. In contrast, no merging shifts occur for hits that occur in the same group. As expected, the 8×8 pad configuration presents the smallest perimeter among all investigated configurations of the same area, hence the highest efficiency. Overall the increase in the pixel group size shows to have a smaller impact on increasing the efficiency, compared to a higher merging frequency. The optimal pixel grouping for optimizing the efficiency was found to be the 8×8 pad grouping which is expected to reach an efficiency up to 99.7%.

A summary of the merging performance for different sensor configurations (group size and merging window) is presented in Table 3. The merging rate is defined as the fraction between hits that are lost or displaced due to merging relative to the total number of hits above threshold. The survival rate shows the number of hits that fall within the spatial tracking cut after a displaced merging event, thus remaining valid. Lastly, the data reduction factor is defined as $R = \left(1 - \frac{N_W}{N_H}\right)$, where N_W is the number of words that are read out from the sensor and N_H is the number of hits above threshold.

As expected, one of the main improvements brought by the increase in group size and decrease in merging window is the reduction of the merging rate. Additionally, the survival rate plays an important role for the detection efficiency of the sensor and depends on the pixel group geometries. For the column-wise pixel group arrangements (2×8, 2×16

Table 3 Summary of the merging performance for different sensor design configurations. The simulation was performed with a uniform 120 GeV/c proton beam

Configuration	Merging rate (displaced and hit loss)	Survival rate	Data reduction factor
2×8, 1.6 ns	2.5%	36.5%	10.6%
2×16, 1.6 ns	2.3%	42.1%	10.7%
2×32, 1.6 ns	2.2%	45.3%	10.8%
8×8, 1.6 ns	1%	0%	11.6%
2×8, 1.0 ns	1.7%	36.1%	7.0%
2×8, 0.5 ns	0.9%	34.6%	3.6%
2×8, 0 ns	0%	N.A.	0%

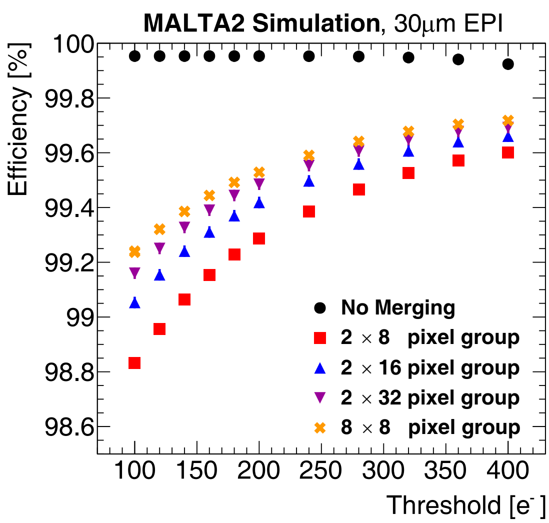

Fig. 17 Simulation of efficiency for various sensor threshold settings. The different curves are related to various pixel groupings in the digital read-out of the sensor. The 2×8 group size corresponds to the digital read-out in the real device, while other pixel groups correspond to possible sensor redesign choices. Additionally, the idealized case of no merging is plotted. All simulation points correspond to a 1.6 ns merging window

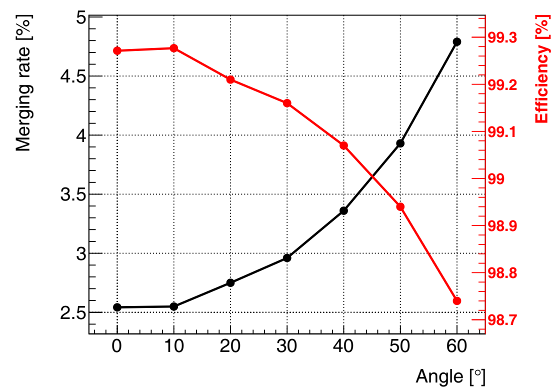

Fig. 18 Simulation of the merging rate (displaced and hit-loss) and detection efficiency for several incident angles of the 120 GeV/c proton beam

and 2×32) the merging in the y-direction is reduced. Consequently, the survival rate increases as it contains a larger fraction of minimal displacement of only 2 pixels on the row-direction. This is however not true anymore for the 8×8 pixel group arrangement which leads to all displaced hits to not be survivable. As expected, the survival rate is not significantly impacted by changes in the merging window. The data reduction factor is seen to increase with larger group configurations and shows a preference for the 8×8 configuration. The increase is small because the average cluster size is ~ 1.5 so that most clusters are contained within a pixel group. The decrease in merging window size leads to a smaller data reduction factor because merging is suppressed.

The effect of different angles of the primary particles on the merging rate was studied in order to gauge the impact of the initial perpendicular beam assumption used in the simulation. Figure 18 shows that as expected the merging rate increases with the beam angle due to an increase in cluster size. An 88% increase in merging rate was observed for an inclination of 60°. In data a similar increase in cluster size with incident angle is seen [11]. The effect of inclination up to 60° on the detection efficiency is less than 0.6%.

5.2 Digital calorimetry application

Digital calorimetry promises a novel energy measurement technique for high energy particle physics [22,23]. The need for high granularity makes MAPS an obvious candidate for such an application. While digital calorimetry expects lower statistical uncertainties on the energy measurement, it also introduces unique challenges in terms of high rate particle counting. This challenge is magnified by the implementation of an asynchronous read-out. Several mitigation techniques are presented that aim to improve the energy reconstruction linearity.

As in the case of the tracking simulation, only primary particles that are perpendicular on the absorber are considered. The secondaries resulting from the electromagnetic shower however are simulated in GEANT4 leading to non-perpendicular incident angles. Similarly to the tracking application, the main source of inefficiency in terms of secondary particle counting is the merging circuit. When only counting

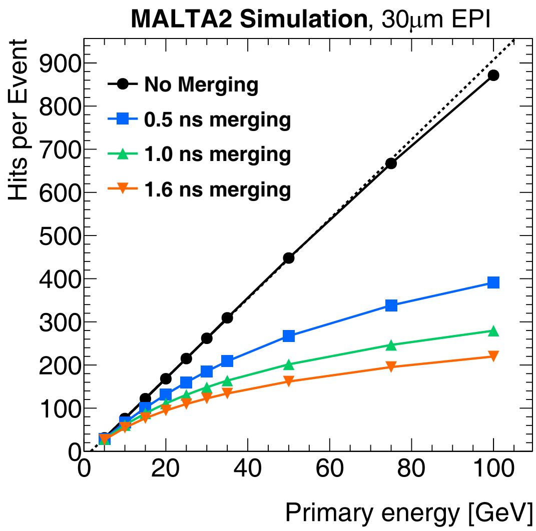

Fig. 19 Simulation of detected number of hits for an incoming electron of variable energy that interacts with a 3.2 cm tungsten block. The different curves correspond to various merging time windows. The time window corresponding to the no merging, functionally denotes the idealized case of a 0 ns merging window. The black dotted line corresponds to a linear fit of the no merging data, performed for electron energies up to 35 GeV. All simulation points correspond to a 2 × 8 pixel grouping

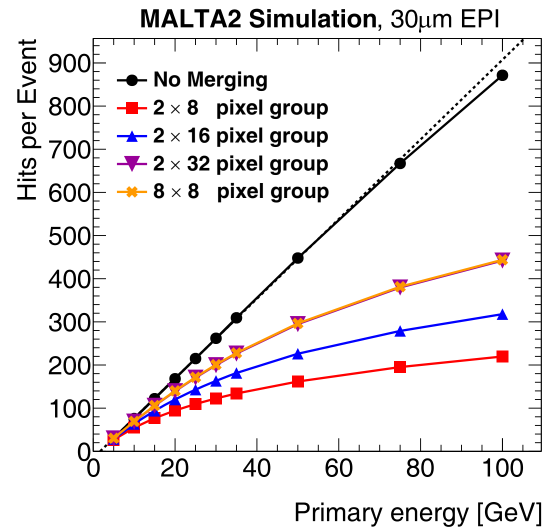

Fig. 20 Simulation of detected number of hits for an incoming electron of variable energy that interacts upon a 3.2 cm tungsten block. The different curves are related to various pixel groupings in the digital read-out of the sensor. The 2 × 8 group size corresponds to the digital read-out in the real device, while other data sets correspond to possible sensor redesign choices. Additionally, the idealized case of no merging is plotted. The black dotted line corresponds to a linear fit of the no merging data, performed for electron energies up to 35 GeV. All simulation points correspond to a 1.6 ns merging window

hits, the hit shifting does not negatively impact the study. In turn, only hit loss merging impacts the energy reconstruction.

Figure 19 shows the simulated mean number of detected hits for each primary particle interaction on a tungsten block. The black curve and points show the idealized case when no merging occurs in the sensor. It records a good linearity up to ∼ 80 GeV. For higher energies, a slight saturation effect can be observed which is explained by the large hit multiplicity that can not be spatially resolved. The orange curve and points show the expected performance for the current sensor design (1.6 ns merging). It highlights that a large hit counting saturation occurs at relatively low energies (< 20 GeV). The decrease in the merging time window gives a clear improvement in terms of the energy measurement linearity, however a significant saturation effect is retained.

The effect of the pixel group size on the simulated number of detected hits is investigated in Fig. 20. A recovery from the saturation effect can be induced with the increase in the pixel group size. In comparison to the tracking application investigated in Fig. 17, the orientation of the pixel grouping does not impact the energy reconstruction. This is highlighted in the 8 × 8 (orange crosses and interpolated line) pixel group arrangement that perfectly matches the 2 × 32 (purple triangles and interpolated line) arrangement. This shows that the merging effect for calorimetry applications is only proportional to the number of pixel group bits. On average the increase of the pixel group size has a larger impact on the counting efficiency of secondary particles.

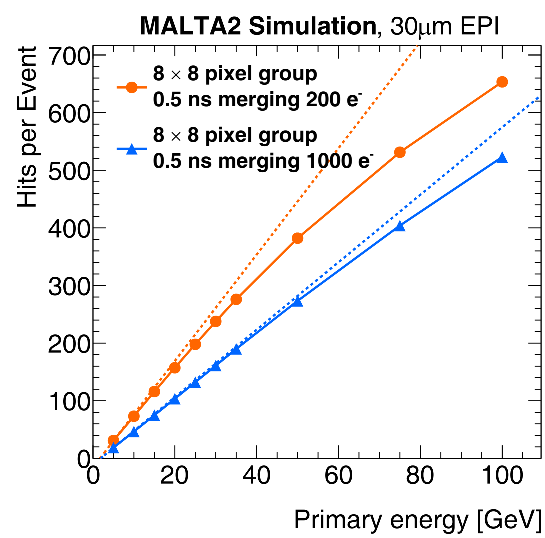

Fig. 21 Simulation of detected number of hits for an incoming electron of variable energy that interacts with a 3.2 cm tungsten block. Two curves are plotted corresponding to a 8 × 8 pixel grouping and a merging window of 0.5 ns. The orange points and interpolated line correspond to a threshold setting of 200 e^- and the blue triangles and interpolated line to 1000 e^-. The dotted lines represent the linear fit of the respective ideal (no merging) data points

Combining the lessons learned from the previous investigations, an optimized design can be proposed: an 8 × 8 pixel grouping with a merging window of 0.5 ns. Figure 21 shows the simulated hit counting linearity for two threshold configurations. The nominal threshold (black line and points) configuration ($200\,e^-$) achieves a good linearity to energies up to 25 GeV. A further increase in the linearity, up to 50 GeV can be achieved by increasing the threshold to $1000\,e^-$. This is due to the smaller number of recorded events, leading to less frequent merging. While a better linearity can be achieved at high energies with an increased threshold, a lower energy resolution is expected at lower energies due to the decreased statistics. The calorimetry performance can be extended to higher energies by implementing a threshold dependent parametrization. A systematic study of both of these effects for a Si-W calorimeter setup with multiple silicon planes is planned to be performed and published in a future paper.

6 Conclusion

A data driven, parametric simulation tool for MAPS-based detectors was developed and presented. The parametrization of the charge sharing was deduced with the help of test beam data on the MALTA2 sensor at the SPS beam line. The simulation has been validated quantitatively and qualitatively in terms of tracking figures of merit: efficiency, average cluster size and cluster timing. An average relative residual between data and simulation of 0.005% was measured for the efficiency and 1.67% for the cluster size. The timing performance has been investigated in terms of the cluster timing. A time resolution of 2.5 ns was obtained for the data and 2.4 ns for the simulation.

The simulation approach allows for a fast and computationally efficient sensor digital design investigation. The main source of inefficiencies in the MALTA2 sensor for both tracking and calorimetry applications was found to be the merging circuit. Improvements for both applications were investigated in terms of silicon sensor redesigns focused on the digital domain.

The leading order improvements on the efficiency have been found to be a decreased merging time window. A secondary order impact was found to be the increase in the pixel group size, with a preference for a grouping that increases the area to perimeter ratio. A mix of such sensor redesigns is expected to increase the efficiency, above a value of 99.8%.

In terms of digital calorimetry, it has been shown that following minor digital redesigns, a single MALTA sensor retains a linear hit counting for electromagnetic showers produced by electrons with energies up to 50 GeV. The electromagnetic showers correspond to the shower maximum, giving a worst case calorimetry estimation. A multi-plane calorimeter expects a better linearity up to higher energies. A systematic study of a multi-layer, fully digital calorimeter for high energy physics is planned in a future work.

The largest improvements in energy reconstruction linearity was found to come from the size of the pixel group. No preference in terms of the pixel group arrangement was found. Additional improvements on the counting linearity were found to be a smaller merging window size and larger thresholds. An optimized design for future calorimetry applications would include a mix or all of these improvements, depending on the physics case.

The successful simulation of MALTA2 sensors enables future large scale detector simulation. A complementary TCAD simulation of MALTA2 sensors is also pursued within the collaboration. Additionally, the implementation of custom read-out circuitry in the simulation is expected to guide future sensor design for tracking and digital calorimetry applications.

Acknowledgements This project has received funding from the European Union's Horizon 2020 Research and Innovation programme under Grant Agreement number 101004761 (AIDAinnova), and number 654168 (IJS, Ljubljana, Slovenia). Furthermore, it has been supported by the Marie Sklodowska-Curie Innovative Training Network of the European Commission Horizon 2020 Programme under contract number 675587 (STREAM).

Data Availability Statement This data will be made available on reasonable request. [Authors' comment: The datasets generated during and/or analysed during the current study are available from the corresponding author on reasonable request.]

Code Availability Statement This code/software will be made available on reasonable request. [Authors' comment: The code is public in this repository. https://gitlab.cern.ch/dberlea/malta_simulation.]

Funded by SCOAP^3.

References

1. M. Munker et al., Simulations of CMOS pixel sensors with a small collection electrode, improved for a faster charge collection and increased radiation tolerance. JINST **14**(05), 05013 (2019). https://doi.org/10.1088/1748-0221/14/05/C05013
2. H. Wennlöf, Simulating monolithic active pixel sensors: a technology-independent approach using generic doping profiles. NIMA **1073**, 170227 (2025). https://doi.org/10.1016/j.nima.2025.170227
3. C. Solans Sanchez et al., Porting MALTA to 65nm (2025). https://cds.cern.ch/record/2918880

4. X. Li et al., Fast timing silicon R&D for the future electron-ion collider. EPJ Web Conf. **316**, 07003 (2025). https://doi.org/10.1051/epjconf/202531607003
5. F. Piro, et al. A 1 μW radiation-hard front-end in a 0.18 μm CMOS process for the MALTA2 monolithic sensor. IEEE Trans. Nucl. Sci. **69**(6), (2022) https://doi.org/10.1109/TNS.2022.3170729
6. G. Gustavino et al., Timing performance of radiation hard MALTA monolithic pixel sensors. JINST **18**(03), 03011 (2023). https://doi.org/10.1088/1748-0221/18/03/C03011
7. M. Dyndal et al., Mini-MALTA: radiation hard pixel designs for small-electrode monolithic CMOS sensors for the High Luminosity LHC. JINST **15**(02), 02005 (2020). https://doi.org/10.1088/1748-0221/15/02/P02005
8. D. Berlea et al., Radiation hardness of MALTA2, a monolithic active pixel sensor for tracking applications. IEEE Trans. Nucl. Sci. **70**(10), 2303–2309 (2023). https://doi.org/10.1109/TNS.2023.3313721
9. L. Fasselt, Charge reconstruction from binary hit data on irradiated MALTA2 Czochralski sensors. NIMA **1080**, 170747 (2025). https://doi.org/10.1016/j.nima.2025.170747
10. L. Fasselt, Charge calibration of MALTA2, a radiation hard depleted monolithic active pixel sensor. NIMA **1082**, 170972 (2026). https://doi.org/10.1016/j.nima.2025.170972
11. D.V. Berlea, Depletion depth studies with the MALTA2 sensor, a depleted monolithic active pixel sensor. NIMA **1063**, 169262 (2024). https://doi.org/10.1016/j.nima.2024.169262
12. L. Fasselt et al., Charge collection parameterization of MALTA2, a depleted monolithic active pixel sensor. JINST **21**(04), 04001 (2026). https://doi.org/10.1088/1748-0221/21/04/C04001
13. S. Meroli et al., Energy loss measurement for charged particles in very thin silicon layers. JINST **6**(06), 06013 (2011). https://doi.org/10.1088/1748-0221/6/06/P06013
14. W. Riegler, G. Aglieri Rinella, Time resolution of silicon pixel sensors. JINST **12**(11), 11017 (2017). https://doi.org/10.1088/1748-0221/12/11/P11017
15. F. Scholze, H. Rabus, G. Ulm, Mean energy required to produce an electron-hole pair in silicon for photons of energies between 50 and 1500 eV. J. Appl. Phys. **84**, 2926–2939 (1998). https://api.semanticscholar.org/CorpusID:55814610
16. M. van Rijnbach et al., Performance of the MALTA Telescope. Eur. Phys. J. C **83**(7), 581 (2023). https://doi.org/10.1140/epjc/s10052-023-11760-z. arXiv:2304.01104
17. M. van Rijnbach et al., Radiation hardness of MALTA2 monolithic CMOS imaging sensors on Czochralski substrates. Eur. Phys. J. C **84**(3), 251 (2024). https://doi.org/10.1140/epjc/s10052-024-12601-3. arXiv:2308.13231
18. M. Kiehn et al., Proteus beam telescope reconstruction (2019). https://doi.org/10.5281/zenodo.2586736
19. G. Ripamonti, Monolithic active pixel sensors based on the TPSCo 65 nm imaging CMOS technology: an overview of results and future challenges. PoS **VERTEX2025**, 034 (2025). https://doi.org/10.22323/1.513.0034
20. C. Lemoine et al., Impact of the circuit layout on the charge collection in a monolithic pixel sensor. JINST **20**(06), 06052 (2025). https://doi.org/10.1088/1748-0221/20/06/C06052
21. ECFA Detector R&D Roadmap Process Group, The 2021 ECFA detector research and development roadmap. Technical report, Geneva (2020). https://doi.org/10.17181/CERN.XDPL.W2EX
22. J. Alme et al., Performance of the electromagnetic pixel calorimeter prototype Epical-2. JINST **18**(01), 01038 (2023). https://doi.org/10.1088/1748-0221/18/01/P01038
23. P. Allport et al., DECAL: a reconfigurable monolithic active pixel sensor for tracking and calorimetry in a 180 nm image sensor process. Sensors (2022). https://doi.org/10.3390/s22186848